

European Electricity Grids May Exhibit Heatwave-induced Capacity Bottlenecks

Enming Liang¹, Minghua Chen^{1,2*}, Srinivasan Keshav^{3*}

¹Department of Data Science, City University of Hong Kong.

²School of Data Science, The Chinese University of Hong Kong (Shenzhen).

³Department of Computer Science and Technology, University of Cambridge.

*Corresponding author(s). E-mail(s): minghua.chen@cityu.edu.hk;

sk818@cam.ac.uk;

Contributing authors: eliang4-c@my.cityu.edu.hk;

12 As climate change increases the frequency, intensity, and duration of heatwaves, under-
13 standing their impact on electricity grids is crucial for enhancing societal security and
14 resilience. We study the effects of heatwaves on European electricity grids using sev-
15 eral comprehensive real-world datasets. Moreover, noting that conventional modeling
16 of temperature effects on grid operation limits is **insufficient** or computationally chal-
17 lenging, we develop a novel **temperature-dependent modeling framework** that is both
18 **comprehensive** and efficient. We apply this method to evaluate the robustness of sev-
19 eral European electricity grids for projected heatwave scenarios for the next **5** years.
20 We identify concerning grid bottlenecks and substantial national differences in vul-
21 nerability: for example, while the Spanish grid exhibits temperature-induced capacity
22 bottlenecks that could jeopardize power supply during heatwaves, the German grid
23 shows remarkable resilience. These findings emphasize the need for temperature-aware
24 grid power flow analysis as well as the need for long-range planning to ensure energy
25 security despite climate-change induced future heatwaves.

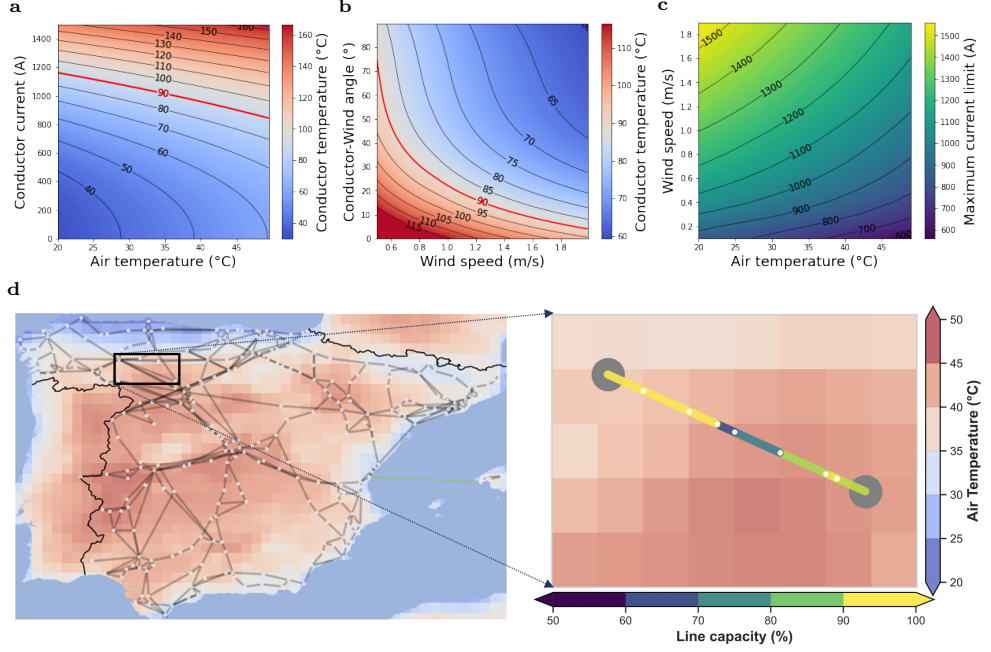


Fig. 1: Heatwaves reduce current capacity and induce transmission line bottlenecks. a-c Physical properties of conductors based on IEEE Std 738TM-2012 under varying weather conditions [1]. a Conductor temperature as a function of air temperature and line current. b Conductor temperature variations with different wind speeds and angles. c Line current capacity under different air temperatures and wind speeds. d Line segment capacity variations along a 130-km transmission line in Northwestern Spain crossing 9 gridded regions, showing localized thermal constraints during heatwaves.

26 Introduction

27 Climate change has led to an increase in average global temperatures, characterized
28 by more frequent, intense, and prolonged heatwaves [2–5]. The escalating frequency
29 and severity of heatwaves impact millions of people worldwide [6] and pose significant
30 challenges to critical infrastructure [7, 8], including electrical power grids [9, 10].
31 A detailed understanding of these impacts on power grid performance is crucial for
32 evaluating and enhancing societal resilience and energy security.

33 Heatwaves create a triple threat to electrical grids. First, they substantially increase
34 cooling demand, driving up electricity consumption [4]. Second, they alter power
35 generation capacity through mechanisms such as wind energy shortages [11] and
36 generator capacity derating [12]. Third, they reduce transmission line capacity as
37 conductors approach their thermal limits (see Fig.1a-c). Moreover, regional variations
38 in weather conditions create spatially heterogeneous thermal constraints along long-
39 distance transmission lines, with different segments experiencing different capacity
40 reductions (Fig.1d).

41 Traditional power flow analyses inadequately capture these heatwave impacts.
42 Existing linearized optimal power flow (OPF) models, even those incorporating
43 weather-dependent dynamic line ratings [13], fail to represent the complex grid dynam-
44 ics that emerge under heavy cooling loads during extreme heat. More critically,
45 they do not precisely model temperature effects on generator capacity derating and
46 the segment-specific thermal constraints of long transmission lines [14]. This over-
47 sight leads to incomplete vulnerability assessments, as our European case studies
48 demonstrate.

49 We address these methodological limitations through a novel framework that
50 combines comprehensive heatwave-aware grid modeling approaches (Fig.2a) with an
51 efficient temperature-dependent alternating-current (AC) OPF analysis under future
52 heatwave projections (Fig.2b). Our approach introduces four key innovations: (i)
53 temperature-dependent electricity demand estimation and generation derating model-
54 ing, (ii) per-segment conductor heat balance modeling to determine thermal-dependent
55 capacity limits for transmission lines, (iii) probabilistic assessment using hundreds of
56 bias-corrected heatwave projections with geospatially-gridded weather profiles, and
57 (iv) an efficient iterative algorithm for temperature-dependent OPF analysis that
58 enables rapid evaluation of national grid resilience across these numerous scenarios.
59 Applying our framework to European electricity grids using publicly available weather
60 profiles, power demand models, renewable penetration scenarios, and grid parameters,
61 we reveal:

62 ▷ We demonstrate that existing grid resilience analyses based on standard AC-
63 OPF approaches fail to adequately capture the combined effects of increased cooling
64 demand and reduced transmission capacity during heatwaves. Even more accurate
65 quadratic approximations for thermal constraints [15] still substantially underestimate
66 transmission line vulnerabilities under extreme heat.

67 ▷ We formulate a temperature-dependent AC-OPF problem that simultaneously
68 incorporates temperature-dependent cooling loads, generator derating, and segment-
69 specific thermally-induced capacity limits for transmission lines, using hundreds of
70 heatwave projections with weather profiles at approximately 30km resolution. We
71 develop a novel iterative algorithm that solves this OPF problem more efficiently while
72 capturing critical nonlinear interactions missed by existing methods.

73 ▷ Applying our framework to European grids reveals significant heatwave vulner-
74 ability. For example, by 2030, up to 4.8% of Spanish transmission lines are projected
75 to drop below 70% of their nominal current-carrying capacity—a typical security
76 constraint margin [16], highlighting the need for heatwave-aware grid management.
77 National-level impacts vary dramatically: the Spanish grid faces substantial load
78 shedding risk under extreme heat, while the German grid demonstrates remarkable
79 resilience. While these findings are based on the best available public data, we caution
80 that further validation with proprietary grid-specific datasets would strengthen these
81 estimations.

82 These findings underscore the urgent need for grid operators and policymakers to
83 consider the impacts of extreme weather more comprehensively in their planning and
84 management strategies. By doing so, they can enhance the reliability and resilience of
85 electricity supplies in the face of increasing climate change challenges.

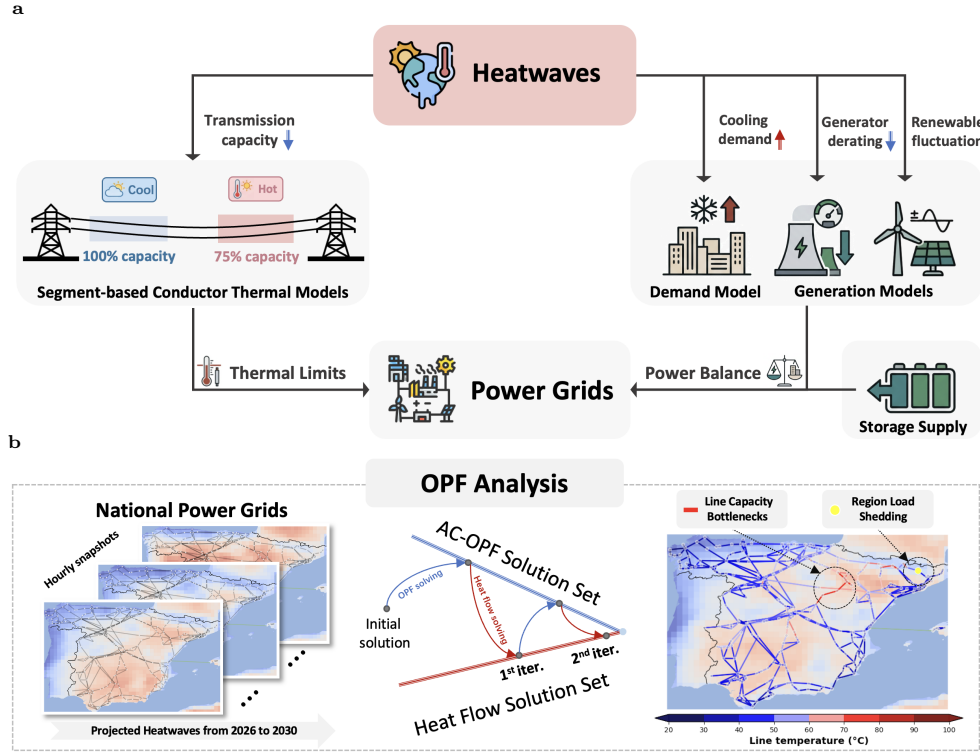


Fig. 2: Framework for analyzing heatwave impacts on national power grids. **a** Integration of segment-specific conductor thermal modeling, temperature-dependent demand, weather-dependent renewable generation, and heatwave-induced generation derating to capture climate-power system interactions. **b** Proposed iterative algorithm solving temperature-dependent AC optimal power flow under bias-corrected heatwave projections, identifying capacity bottlenecks and potential load shedding regions during extreme heat events.

86 Results

87 Setup

88 We employ the modeling framework illustrated in Fig. 2a, with data source and
 89 detailed methods included in Section 1, to evaluate how heatwaves impact [existing](#) grid
 90 operations in European countries under [projected future](#) heatwave scenarios. We focus
 91 [our analysis on 2026–2030](#), a time horizon that reduces uncertainty in both climate
 92 projections and grid infrastructure configurations while providing [actionable insights](#)
 93 for near-term resilience planning and investment decisions. We conduct optimal power
 94 flow (OPF) analyses using the proposed iterative algorithms in Fig. 2b, to investigate
 95 whether national grids exhibit temperature-induced capacity bottlenecks, [indicated by](#)
 96 [transmission lines approaching their thermal limits](#) and load-shedding regions—that
 97 is, buses where power injection fails to meet consumption. Our work also compares the

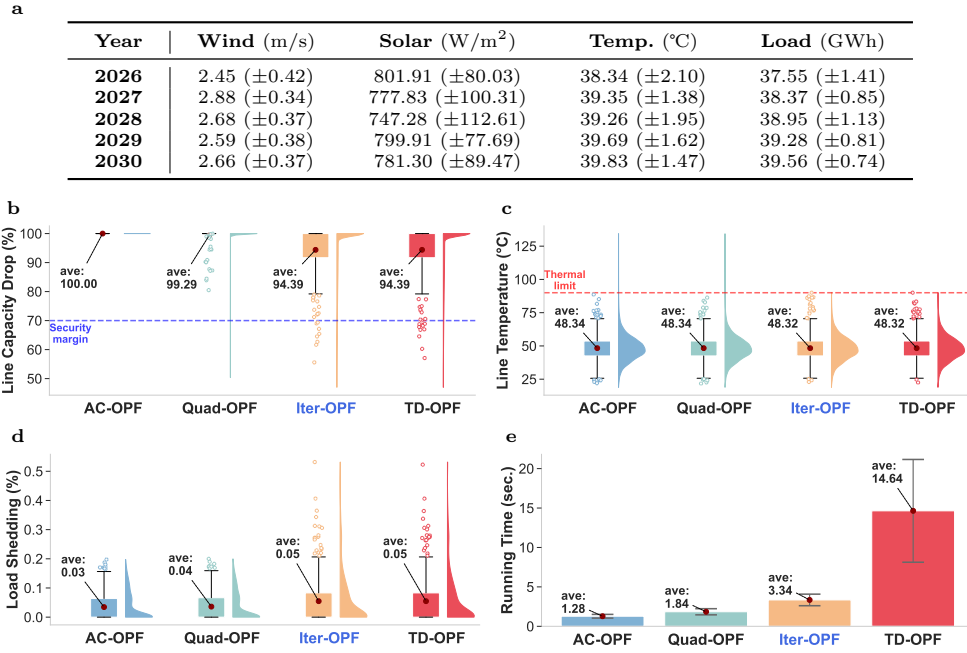


Fig. 3: Comparison of different OPF methods for analyzing the Spanish grid under projected heatwaves. We compare basic AC-OPF, advanced Quad-OPF, our proposed Iter-OPF, and the most accurate TD-OPF. **a** Weather and load statistics under heatwave projections from 2026 to 2030, with 320 scenarios generated using a bias-correction approach (detailed in Section 1.1). **b–c** Distributions of estimated line capacity reduction compared to nominal conditions and line temperatures (derived from heat balance equations) across different methods. **d** Distributions of load shedding ratios (demand-generation mismatch over total demand). **e** Average per-scenario solving times.

98 accuracy of existing OPF analysis methods with our proposed approach in identifying
99 these critical bottlenecks while satisfying physical constraints.

100 Observations

101 We find that, as heatwaves simultaneously reduce transmission capacity, [cause generator derating](#),
102 and increase cooling demand, some European national grids, [such as Spain, France, and Italy](#), exhibit capacity bottlenecks in projected heatwave scenarios,
103 subsequently resulting in non-negligible load-shedding and potential human casualties [17, 18]. This alerting observation emphasizes the need for temperature-aware grid
104 analysis and planning to mitigate heatwave risks and ensure energy security. In further
105 detail, we have the following observations:
106

108 Existing OPF models overestimate grid resilience under heatwaves

¹⁰⁹ We compare four OPF-based approaches: the standard alternating current OPF (AC-
¹¹⁰ OPF), a more advanced ACOPF with quadratic approximation of thermal limits
¹¹¹ (Quad-OPF), our proposed iterative framework (Iter-OPF), and the most accurate
¹¹² fully converged temperature-dependent ACOPF (TD-OPF). Detailed formulations are
¹¹³ in Section 1.5 and [Supplementary Section 2](#).

¹¹⁴ Conventional methods substantially underestimate heatwave risks. AC-OPF
¹¹⁵ neglects thermal limits entirely, while Quad-OPF’s quadratic approximation fails to
¹¹⁶ precisely capture the complex nonlinear relationship between temperature and current-
¹¹⁷ carrying capacity (Fig.3b). Both methods permit line temperatures to exceed the
¹¹⁸ 90°C thermal limit (Fig.3c), overestimating transmission capacity and underestimating
¹¹⁹ load shedding (Fig.3d). Implementing generation plans based on these methods
¹²⁰ during heatwaves could trigger line shutdowns or even cascading blackouts [17, 18].

¹²¹ Our Iter-OPF framework addresses these limitations. Like TD-OPF, it correctly
¹²² identifies load shedding regions and maintains safe line temperatures below 90°C.
¹²³ Yet while TD-OPF requires over four times the computational cost of AC-OPF
¹²⁴ (Fig. 3e), Iter-OPF achieves comparable accuracy at only twice the cost, enabling reliable
¹²⁵ resilience assessment across hundreds of weather scenarios for comprehensive grid
¹²⁶ planning.

¹²⁷ **Complete thermal modeling is essential for accurate resilience ¹²⁸ assessment under heatwaves**

¹²⁹ To assess the importance of different modeling components under heatwaves, we
¹³⁰ conduct an ablation study systematically removing key elements from Iter-OPF:
¹³¹ conductor thermal models, segment-based modeling, and generator derating (Fig.4a–
¹³² b). We also compare these against the widely used 70% security margin SC-OPF
¹³³ approach [16].

¹³⁴ Conductor thermal modeling proves most critical. Removing it substantially
¹³⁵ overestimates grid capacity, while segment-based modeling captures local thermal bot-
¹³⁶ tlenecks that uniform approaches miss (Fig. 4a). Generator derating has comparatively
¹³⁷ smaller impacts on system-level performance.

¹³⁸ The 70% security margin approach [16], though commonly used, only partially
¹³⁹ prevents line overheating (Fig. 4b). This fixed margin cannot avoid thermal violations
¹⁴⁰ because it neglects spatial heterogeneity in thermal conditions—actual capacity
¹⁴¹ can drop near 40% of nominal ratings during extreme heatwaves in localized hotspots
¹⁴² (Fig.3d). These results demonstrate that explicit temperature-dependent thermal
¹⁴³ modeling is essential; conservative static margins alone are insufficient for reliable
¹⁴⁴ heatwave resilience assessment.

¹⁴⁵ **Rising demand amplifies grid stress, yet energy storage alone ¹⁴⁶ offers limited relief**

¹⁴⁷ We assess grid resilience sensitivity to future demand growth and energy storage
¹⁴⁸ availability. With load growth rates from 1% to 3% annually from 2025, reflecting
¹⁴⁹ emerging demands from AI infrastructure, electrified heating and cooling, and electric
¹⁵⁰ vehicles [19, 20], load shedding increases proportionally with demand (Fig. 4c). This

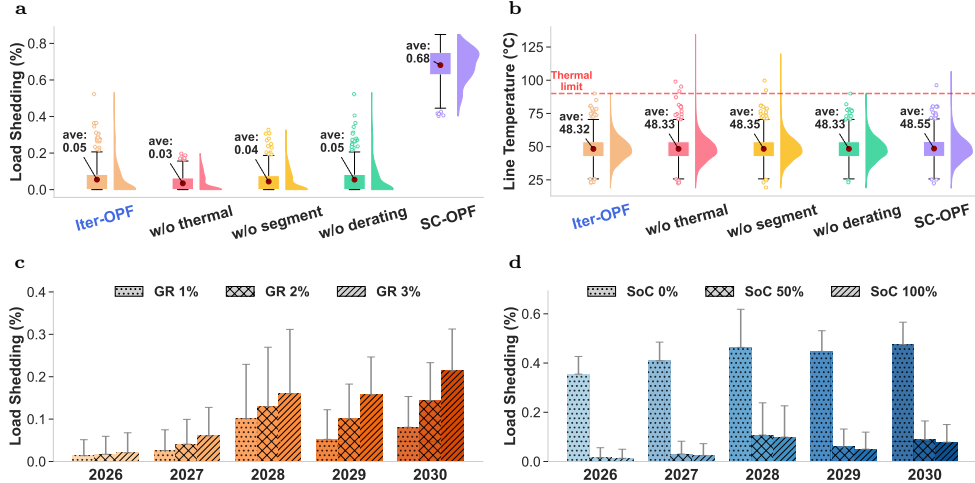


Fig. 4: Sensitivity analysis of modeling components and environmental factors on OPF analysis under heatwaves. a–b Impact of removing different modeling components from the Iter-OPF framework on load shedding ratios and line temperatures, compared to the 70% security margin SC-OPF method [16]. c–d Load shedding ratios under different load growth rates (GR) and energy storage states (i.e., SoC).

positive relationship reveals that rising consumption patterns will directly amplify grid stress during heatwaves.

On the other hand, varying energy storage state-of-charge (SoC) from 0% to 100% yields only marginal reductions in load shedding (Fig. 4d). This counterintuitive result arises because transmission constraints—not generation capacity—dominate grid vulnerability during extreme heat. Higher storage availability cannot compensate when reduced line capacity prevents power delivery from storage units to demand centers. This finding indicates that expanding the capacity of existing storage infrastructure alone cannot adequately mitigate heatwave impacts. Planning must combine transmission upgrades and distributed flexibility to address thermal constraints directly.

162 **Grid vulnerability differs by country and cross-border ties are not 163 always helpful**

Grid vulnerability to heatwaves varies dramatically across eight Western European countries. French electricity grid shows severe thermal-induced capacity bottlenecks during extreme heat, with average load shedding reaching 2% under projected heatwaves (Fig. 5a), potentially causing widespread power disruptions [17]. In contrast, Germany, the UK, and other northern countries maintain full supply without load shedding under the same projected scenarios (Fig. 5b).

Cross-border interconnections provide asymmetric benefits depending on neighboring grid conditions. France experiences substantial relief from power sharing with less-stressed neighbors—load shedding decreases by about 2% when interconnected

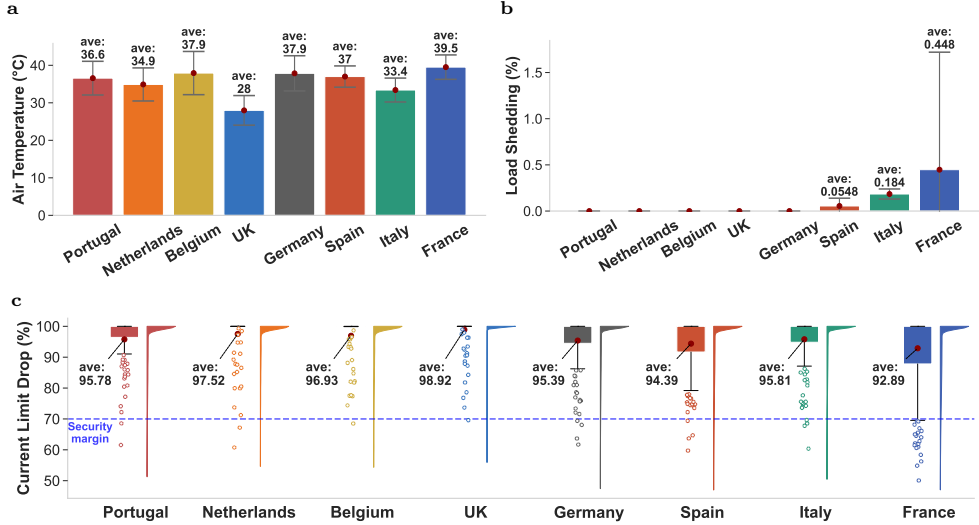


Fig. 5: National grids in Western Europe, such as France, Italy, and Spain, exhibit substantial load shedding under projected heatwaves, while other countries remain resilient. **a** Average air temperature during the hottest hours in projected heatwave periods. **b** Average load shedding across different countries. **c** Distribution of line capacity reduction compared to nominal ratings during heatwaves.

173 with Italy (Fig. 6b,d). Conversely, joint simulations of Spain with Portugal or France
 174 show minimal relief because France faces similar thermal stress during concurrent
 175 heatwaves and also because limited transmission capacity constrains power delivery
 176 to stress centers (Fig. 6a,c). This disparity arises because interconnection effective-
 177 ness depends on the spatial correlation of climate stress, available surplus capacity in
 178 neighboring systems, and sufficient transmission infrastructure to deliver power where
 179 needed.

180 These findings highlight that climate-resilient grid planning requires coordinated
 181 European strategies. Countries facing severe thermal constraints need targeted infras-
 182 tructure upgrades—particularly transmission capacity and cooling systems—while
 183 strategic interconnections can provide mutual support where climate impacts are
 184 spatially decorrelated.

185 Broader Implication

186 Our findings have immediate implications for European energy policy. Grid operators
 187 should periodically re-evaluate resilience assessments using temperature-dependent
 188 methodologies and the latest climate projections. Policymakers should combine
 189 transmission upgrades in thermally vulnerable corridors—particularly in southern
 190 Europe—rather than relying solely on storage expansion or demand response. The
 191 spatial correlation of climate stress across borders further underscores the need for
 192 pan-European coordination; interconnection benefits depend critically on whether
 193 neighboring systems face concurrent thermal constraints.

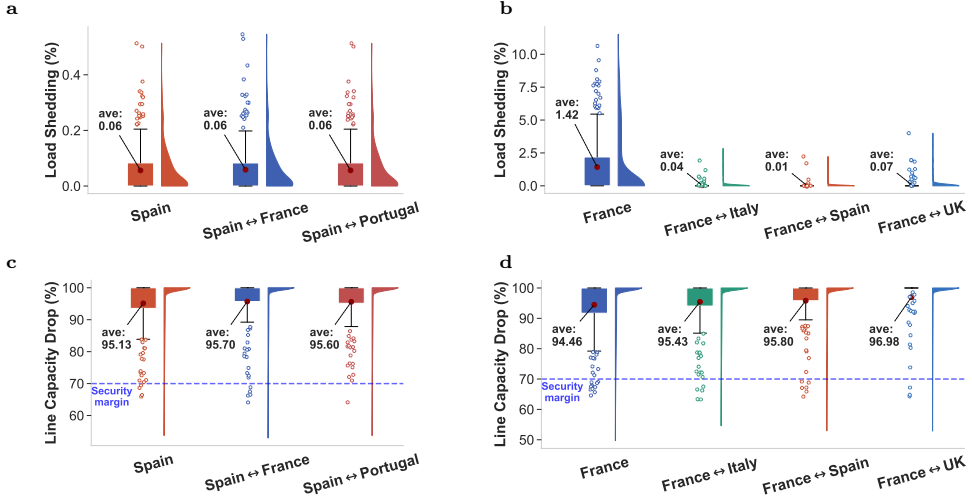


Fig. 6: Cross-border interconnections enhance grid resilience by enabling mutual support during heatwaves. We compare single-country analyses with joint multi-country analyses under identical heatwave projections to quantify the effects of cross-border interconnections on grid resilience. **a–b** Distribution of Load shedding ratio in Spain and France across different interconnection scenarios. **c–d** Distribution of Line capacity reduction in Spain and France across different interconnection scenarios.

194 Limitations

195 Whilst concerning, we note that our results rely on publicly available datasets for
 196 European grids, which lack the granular detail accessible to grid operators. Additionally,
 197 although we use the best currently available locally bias-corrected weather
 198 projections [21], these remain subject to revision as climate models improve. Similarly,
 199 projecting cooling load patterns involves inherent uncertainties stemming from
 200 evolving building efficiency standards, air conditioning adoption rates, and demand
 201 response capabilities.

202 We focus on near-term scenarios (2026–2030) to reduce forecasting uncertainty;
 203 longer-term climate impacts and grid vulnerabilities may be more severe. However,
 204 future grid evolution—including increased renewable energy penetration, trans-
 205 mission capacity upgrades, energy storage deployment, and other infrastructure
 206 improvements—remains uncertain and could substantially alter these vulnerability
 207 projections [22]. Our analysis, therefore, represents current grid configurations under
 208 near-term climate scenarios rather than a long-term forecast of grid performance.

209 Our iterative algorithm has been validated against the fully converged TD-OPF
 210 model, demonstrating numerical consistency with the underlying physical models.
 211 However, the TD-OPF model itself has not been validated against real-world field
 212 tests of line temperatures during heatwave events. Errors in the underlying physical
 213 model or biased input data will propagate through our analysis.

214 Given these limitations, grid operators should validate our findings against histori-
215 cal outage records and apply our methodology with their proprietary, higher-resolution
216 models and real-time operational data for more precise vulnerability assessments.

217 Discussion and Conclusion

218 Extreme heat poses a compound threat to electrical grids—simultaneously increasing
219 cooling demand, reducing generation efficiency, and degrading transmission capacity.
220 Yet existing assessment methods fail to capture these coupled dynamics or provide the
221 computational efficiency needed for probabilistic analysis across numerous climate sce-
222 narios. Current models also overlook the spatially heterogeneous, weather-dependent
223 thermal limits along individual transmission line segments.

224 We address these gaps with a framework integrating thermal modeling across
225 demand, generation, and transmission with geospatially-gridded climate projections.
226 Our iterative algorithm efficiently solves the temperature-dependent optimal power
227 flow problem while incorporating segment-specific thermal limits, capturing critical
228 nonlinear interactions that existing methods miss. Applying this framework to West-
229 ern European grids reveals substantial variation in national resilience: Germany’s
230 grid can withstand projected extreme heat, while Spain and France face significant
231 vulnerability to supply disruptions.

232 The heatwave-induced capacity bottlenecks identified by our work can be mit-
233 iated through three complementary approaches. First, demand response programs
234 in affected load centers can maintain grid integrity, though at the cost of consumer
235 inconvenience. Second, reconductoring vulnerable transmission lines—which our anal-
236 ysis specifically identifies—can increase capacity and resilience, though this requires
237 capital investment and significant lead time. Third, deploying grid-scale storage at
238 bottleneck locations could compensate for transmission limits during extreme heat
239 events, an approach that warrants investigation as storage costs continue to decline.

240 *Climate change is accelerating while grid infrastructure evolves slowly. The meth-*
241 *ods and findings presented here provide a foundation for prioritizing adaptation*
242 *investments before the next extreme heatwave tests grid limits. Future work should*
243 *extend our framework to optimize adaptation investments under climate uncertainty,*
244 *incorporating cost-benefit analysis and long-term climate trajectories. Our analysis*
245 *relies on diverse datasets, not all of which are easy to obtain or process, such as*
246 *country-specific calibrated demand models. To support reproducibility and enable*
247 *broader application, we openly share our datasets, algorithms, and source code.*

248 1 Methods

249 Data Sources

250 We employed multiple publicly available datasets covering European transmission
251 infrastructure, climate conditions, power demand, and renewable generation. The
252 European transmission network topology and parameters were derived from PyPSA-
253 Eur [16], an open-source model of the European energy system. Algorithm validation

used standardized IEEE power flow benchmarks from PGLIB [23]. Historical climate data were obtained from ERA5 [24], providing hourly meteorological fields at $0.25^\circ \times 0.25^\circ$ resolution from 1940 to present. Future climate projections were sourced from the Copernicus Climate Change Service Energy dataset [25], covering 2005–2100 with temperature, solar irradiance, and wind velocity fields. Historical electricity demand profiles were extracted from ENTSO-E Power Statistics [26]. Weather-dependent demand variations were modeled following Demand.ninja [27]. Renewable generation potentials and time series were computed using Atlite [28].

Comprehensive dataset descriptions are provided in [Supplementary Table 1](#).

Models and Algorithms

We developed a comprehensive framework to assess transmission grid resilience under extreme heatwaves, integrating heatwave projection, demand modeling, and optimal power flow analysis. As depicted in Fig. 2, the framework comprises:

- **Future Heatwave Projection (Sec. 1.1):** Generates [multiple](#) projected heatwave events for 2025–2030 based on historical events from 2019 and 2022.
- **Future Demand Modeling (Sec. 1.2):** Simulates power demand under varying annual growth rates using a weather-dependent model from Demand.ninja [27].
- **Generator Derating Modeling (Sec. 1.3):** Quantifies reduced generator efficiency due to elevated ambient temperatures during heatwaves.
- **Renewable Generation:** Calculates renewable generation potential under projected weather conditions using Atlite [28].
- **Transmission Line Thermal Modeling (Sec. 1.4):** Quantifies temperature effects on conductor properties and thermal limits, [including multi-bundle line derating and segmented analysis to identify localized stress points](#).
- **Optimal Power Flow Analysis (Sec. 1.5):** Integrates these components to simulate grid response under thermal and demand stresses, revealing critical capacity constraints and vulnerability zones.

1.1 Future Heatwave Modeling

We adopt future reference climate variables based on the bias-corrected European regional climate model, CORDEX, under the RCP 4.5 scenario for the European domain [25]. However, these reference climate data are averaged over three-hour intervals and lack prediction uncertainty intervals, thus inadequately capturing shorter-duration extreme heat events.

To address this limitation, we apply a “morphing” approach to artificially create future heatwaves based upon historical weather observations [29, 30]. This approach preserves the spatial structure and diurnal patterns of historical heatwaves while shifting the temperature baseline, though it assumes that heatwave dynamics will remain qualitatively similar under future climate conditions. This approach has often been used for the analysis of building energy use or assessing resilience under different future climate scenarios [31].

We first select temperature profiles from historical heatwave events in the [hourly](#) ERA5 reanalysis dataset, denoted as $T_{\text{heat}}^{\text{his}}$, and the historical reference temperature

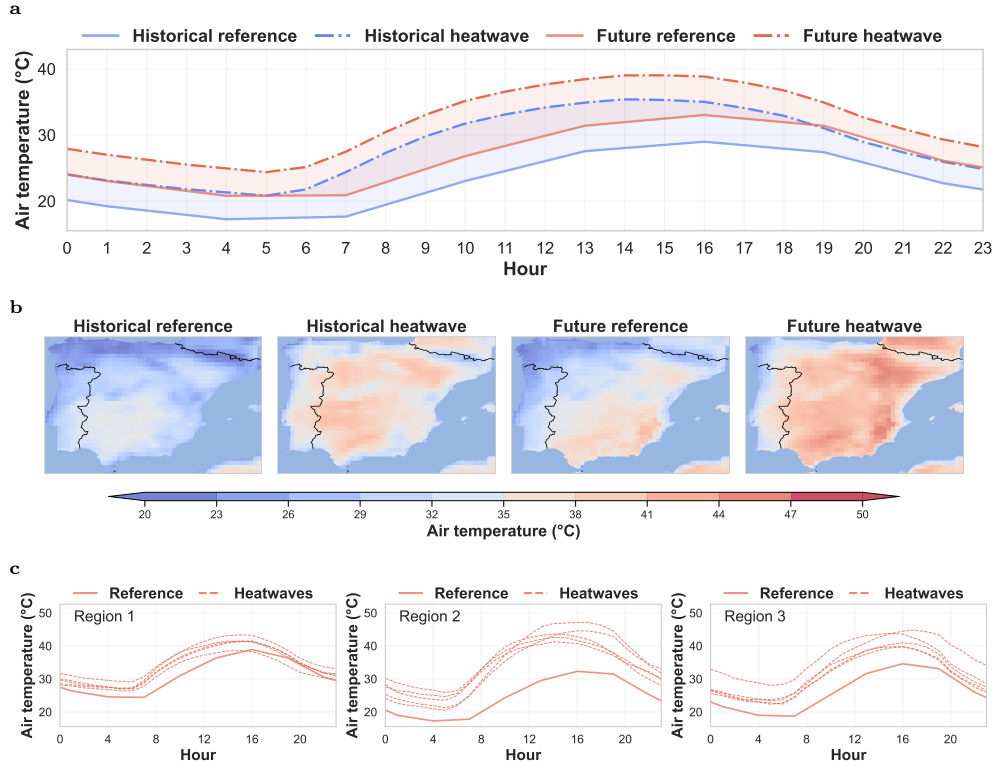


Fig. 7: Projected 2030 heatwaves in Spain derived from 2022 observations. **a** Morphing approach for projecting future heatwaves. Delta values calculated from a historical heatwave day are applied to a future reference day to generate projected conditions. Temperature values represent spatial averages across regions. **b** Spatial characteristics of generated heatwaves compared to historical events and reference profiles. The morphing approach preserves spatial and temporal patterns from historical events. **c** Generated 2030 heatwaves based on delta values from five historical hottest days in July 2022. Profiles for three areas are shown separately.

296 data, $T_{\text{ref}}^{\text{his}}$, on the same historical date. To derive the projected future **hourly** heat-
 297 wave scenarios $T_{\text{heat}}^{\text{fut}}$ from the future reference temperature $T_{\text{ref}}^{\text{fut}}$, we calculate it as
 298 $T_{\text{heat}}^{\text{fut}} = T_{\text{ref}}^{\text{fut}} + (T_{\text{heat}}^{\text{his}} - T_{\text{ref}}^{\text{his}})$, where the low-resolution 3-hourly reference data is linearly
 299 **interpolated to generate a complete 24-hour time series for this calculation.**

300 The projected future heatwave exhibits a similar temperature increase relative
 301 to the historical reference (Fig 7a) while preserving the spatial features at each
 302 longitude-latitude grid (Fig 7b). Furthermore, we collect a set of such bias values (i.e.,
 303 $(T_{\text{heat}}^{\text{his}} - T_{\text{ref}}^{\text{his}})$) based on different historical heatwave records, to present a historical
 304 distribution of extreme weather patterns (Fig 7c). This approach allows us to capture
 305 the diversity of potential heatwave manifestations while maintaining their inherent
 306 spatial characteristics in our future projections.

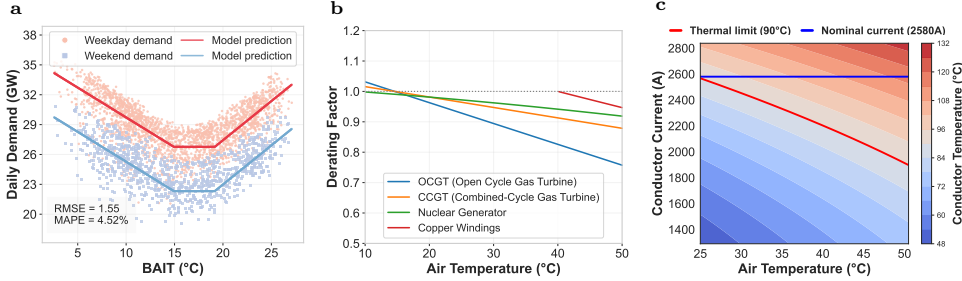


Fig. 8: Heatwave impacts on load demand, generator efficiency, and transmission capacity. a Calibrated temperature-dependent demand model for Spain following Demand.ninja [27], where BAIT indicates building-adjusted internal temperature depending on multiple weather variables. b Generator derating model for various common generators, where higher ambient temperature induces lower generation efficiency due to different mechanisms. c Conductor thermal models based on heat balance equations, where the nominal current capacity is determined under thermal limits in ambient conditions; as air temperature increases, the current limits decrease.

307 1.2 Future Demand Modeling

308 We employ a weather-dependent demand model following Demand.ninja [27] to
 309 simulate future daily demand as follows:

$$P^d = P_{\text{base}} + P_{\text{heat}}[T_{\text{heat}} - \text{BAIT}]^+ + P_{\text{cool}}[\text{BAIT} - T_{\text{cool}}]^+ + \alpha W + \beta D + \epsilon,$$

310 where base load P_{base} denotes the base demand (in GW), P_{heat} and P_{cool} are heating
 311 and cooling coefficients (in $\text{GW}/^{\circ}\text{C}$), T_{heat} and T_{cool} are heating and cooling thresholds
 312 (in $^{\circ}\text{C}$), and BAIT denotes the building-adjusted internal temperature derived from
 313 [27], which depends on specific weather conditions such as air temperature, relative
 314 humidity, wind speed, and solar radiation. α is a time-dependent coefficient (in GW),
 315 representing the impacts of differences in workdays ($W = 1$) and weekends ($W = 0$),
 316 β (in GW/yr) captures the long-term yearly trends in power demand, and ϵ is the
 317 model error term. After generating daily power demand, we convert it to an hourly
 318 resolution based on the historical average hourly demand ratios observed during hot
 319 days, following [27].

320 We follow the methodology [27] to calibrate demand models for EU countries
 321 in our case study. For future scenarios, we incorporate varying annual growth rates
 322 (β) to model different load projections. This approach accounts for unprecedented
 323 grid challenges from AI technologies, smart homes, and electric vehicles, which will
 324 significantly alter historical demand patterns [19, 20]. By adjusting these growth rates,
 325 we evaluate grid performance under various electrification scenarios, from moderate
 326 to aggressive technology adoption.

327 1.3 Generator Derating Modeling

328 Heatwave-induced high temperatures also derate generator capacity. For renewable
 329 generators, such as solar generation, the Atlite package [28] is employed to convert
 330 weather data into renewable power generation profiles. For Gas Turbines (GT)

331 and Combined-Cycle Gas Turbines (CCGT), the density of input air decreases with
 332 increasing ambient temperature, resulting in more fuel needed to compress the same
 333 amount of air mass [12]. Nuclear power generators experience capacity decreases at
 334 high temperatures due to their reliance on water cooling systems to prevent overheating
 335 [32]. For Electric Generators with copper windings, elevated temperatures increase
 336 winding resistance, inducing Joule heating and reducing efficiency [33]. We then sum-
 337 marize the capacity derating factor $\eta \leq 1$ for some conventional generators under
 338 ambient temperatures T_{amb} using:

$$\text{Generator derating } \eta = \begin{cases} (-0.6854T_{\text{amb}} + 110)/100 & (\text{GT}) \\ (-0.3427T_{\text{amb}} + 105)/100 & (\text{CCGT}) \\ (101.3042 - 0.1387T_{\text{amb}} - 0.0010T_{\text{amb}}^2)/100 & (\text{Nuclear}) \\ \sqrt{\frac{(180 - T_{\text{amb}})[1 + 0.0039(40 - 20)]}{(180 - 40)[1 + 0.0039(\frac{T_{\text{amb}} - 20}{40})]}} & (\forall T_{\text{amb}} \geq 40) \text{ (Copper windings)} \end{cases}$$

339 These coefficients of derating curves depend on the detailed manufacturing configu-
 340 rations of different generators and can be adjusted under different real-world systems
 341 [12, 32, 33].

342 1.4 Conductor Thermal Modeling

343 Heatwaves also reduce transmission capacity in power grids by affecting the thermal
 344 behavior of overhead conductors. This physical phenomenon can be modeled by the
 345 steady-state heat balance equation, which accounts for the equilibrium between heat
 346 generated by electrical current and solar radiation, and heat lost through convection,
 347 radiation, and conduction.

348 Heat Balance Equations

349 The standard steady-state heat balance equation according to IEEE Std 738TM-2012
 350 [1] used in our study is as follows:

$$\underbrace{H_C + H_R}_{\text{heat loss}} = \underbrace{H_S + H_J}_{\text{heat gain}} \quad [\text{W/m}], \quad (1)$$

351 where

$$H_C = \max \begin{cases} 3.645\rho_f^{0.5}D^{0.75}(T - T_{\text{amb}})^{1.25}, & (\text{zero wind speed}); \\ K_\phi [1.01 + 1.35N_{\text{Re}}^{0.52}] \lambda_f (T - T_{\text{amb}}), & (\text{low wind speed}); \\ 0.754K_\phi N_{\text{Re}}^{0.6} \lambda_f (T - T_{\text{amb}}), & (\text{high wind speed}); \end{cases}$$

$$H_R = \pi\sigma_B D\alpha_{\text{emi}} \left[(T + 273)^4 - (T_{\text{amb}} + 273)^4 \right]$$

$$H_S = \alpha_{\text{abs}} DS$$

$$H_J = I^2 R(T) = I^2 R_{\text{ref}}(1 + \alpha_r(T - T_{\text{ref}}))$$

352 Here, given the conductor physical properties (conductor diameter D , emissivity
 353 factor α_{emi} , absorptivity factor α_{abs} , resistance coefficient α_r , unit reference resistance
 354 R_{ref}) and environmental variables (conductor temperature T , ambient temperature
 355 T_{amb} , air density ρ_f , air thermal conductivity λ_f , wind angle factor K_ϕ , Reynolds
 356 number N_{Re} , solar radiation S , and constant δ_B), the heat balance equation solves
 357 for the equilibrium conductor temperature that balances heat inflow and outflow.

358 The heat transfer components include convective heat loss H_C , radiative heat loss
 359 H_R driven by temperature difference, solar heat gain H_S , and Joule heat gain H_J
 360 from conductor current I and temperature-dependent unit resistance $R(T)$. Detailed
 361 parameter definitions are provided in [Supplementary Table 7](#).

362 For simplicity, we denote the implicit mapping from conductor current to equilib-
 363 rium conductor temperature as $T = \mathcal{H}(I, \mathcal{W})$, where \mathcal{W} includes all environmental
 364 variables shown above, such as air temperature and wind speed. We remark that the
 365 mapping from current to equilibrium temperature is a single-variable monotonic map-
 366 ping, i.e., higher current leads to higher conductor temperature given identical weather
 367 variables. Thus, it can be efficiently solved using the bisection or Newton's method.

368 Multi-Bundle Modeling

369 In practice, multi-bundle transmission lines are commonly used for high-voltage trans-
 370 mission grids, which complicates thermal modeling due to mutual interactions between
 371 conductor bundles. Conductors within a bundle experience reduced cooling when posi-
 372 tioned in the wake of neighbors, with finite-element simulations showing temperature
 373 variations of 5–25°C between individual bundles in common four-bundle transmission
 374 lines [34]. Two simplified modeling approaches are commonly used. Individual con-
 375 ductor modeling treats each bundle independently, overestimating capacity by neglecting
 376 mutual thermal shielding [16]. Merged conductor modeling combines bundles into a
 377 single equivalent line, underestimating capacity by ignoring inter-bundle convective
 378 cooling.

379 Following finite-element analysis results showing 5–25°C temperature elevations
 380 in shielded conductors within four-bundle configurations [34], we apply a reduction
 381 factor of 0.8 to convective and radiative cooling terms as $0.8(H_C + H_R) = H_S +$
 382 H_J . Specifically, under worst-case ambient conditions (0.6 m/s wind, 900 W/m² solar
 383 irradiance) [35], this predicts the 90°C thermal limit at 25°C ambient temperature,
 384 falling between the two simplified approaches with approximately 15°C difference from
 385 the optimistic individual conductor model, consistent with finite-element simulations
 386 showing temperature variations of 5–25°C [34]. This approximation captures inter-
 387 bundle thermal shielding effects without requiring computationally expensive finite-
 388 element simulations for each line segment.

389 Multi-Segment Modeling

390 Heatwaves further induce spatially heterogeneous effects on grid transmission capacity,
 391 especially for long-distance transmission lines. To capture these varied impacts, we
 392 compute the intersection of transmission lines with grid lines embedded in weather
 393 datasets such as ERA5 (see Fig. 1b). Segments within a single grid cell share the power
 394 flow and current, but have different resistances due to thermal effects under various
 395 local weather conditions, such as wind speed and solar radiation. For each link, the
 396 multi-segment model satisfies the following equations:

$$\text{Heat balance equations } T_{l,s} = \mathcal{H}(I_l, \mathcal{W}_{l,s}), \forall s \in \mathcal{S}_l \quad (2)$$

$$\text{Conductor thermal limits } T_{l,s} \leq T^{\max}, \forall s \in \mathcal{S}_l \quad (3)$$

$$\text{Transimision line resistance } R_l = \sum_{s \in \mathcal{S}_l} d_{l,s} \cdot R(T_{l,s}), \quad (4)$$

397 The conductor temperature for each segment $s \in \mathcal{S}_l$ from line l in Equation (2) is
 398 derived from the heat balance equation (Equations (1)) based on local weather con-
 399 ditions. Segment temperature $T_{l,s}$ is constrained by the transmission line's thermal limit
 400 T^{\max} (e.g., 90°C for ACSR conductors) in Equation (3). The total line resistance equals
 401 the sum of segment resistances as shown in Equation (4), where $d_{l,s}$ is the segment's
 402 length and $R(T)$ is the temperature-dependent unit resistance. Consequently, branch
 403 flow is limited by the segment with the highest temperature. This approach is com-
 404 patible with any gridded weather dataset, allowing our segmented transmission model
 405 to automatically improve in accuracy as weather data becomes more fine-grained.

406 The comprehensive formulations and discussions for the above thermal models are
 407 included in [Supplementary Section 4.4](#).

408 1.5 Optimal Power Flow Analysis

409 The Optimal Power Flow (OPF) problem is a fundamental component in electricity
 410 grid operations and vulnerability analysis. It aims to determine the most efficient oper-
 411 ating conditions for an electrical power system, ensuring that power generation meets
 412 the demand while minimizing operational costs and adhering to system constraints.

413 For different planning horizons, power grid optimization can be categorized into
 414 three types: (1) planning problem, which addresses long-term infrastructure devel-
 415 opment decisions over years to decades; (2) short-term set-point dispatching, which
 416 focuses on day-ahead to hour-ahead scheduling of generation resources; and (3)
 417 real-time control, which manages immediate system adjustments within minutes to
 418 maintain stability and reliability. Each timescale presents distinct objectives, con-
 419 straints, and computational requirements while sharing the fundamental goal of
 420 optimal resource allocation.

421 In the context of grid vulnerability analysis, we employ hourly single-snapshot
 422 OPF simulations to systematically identify grid bottlenecks during extreme weather
 423 events. By solving the OPF problem at each hour during extreme periods, we can
 424 pinpoint transmission lines, generators, and other components that consistently reach
 425 their operational limits, representing critical vulnerabilities in the system. This tem-
 426 poral granularity allows us to capture the dynamic nature of both electricity demand
 427 patterns and environmental impacts, particularly during heatwaves when thermal
 428 constraints become increasingly binding.

429 We first introduce the standard single-snapshot alternating-current OPF (AC-
 430 OPF) problem in Sec. 1.5 and extend to include conductor thermal modeling in
 431 Sec. 1.5, contingency security constraints in Sec. 1.5, and optimization with storage
 432 units in Sec. 1.5.

433 **Baseline OPF Methods.** To our knowledge, the most standard OPF formulation
 434 based on the Alternating Current (AC) model is AC Optimal Power Flow (AC-OPF)
 435 [36]. It is a non-linear, constrained optimization problem that incorporates both the
 436 physical laws governing power flow and the operational limits of the grid compo-
 437 nents. Given hourly load demand $\{\mathbf{P}^d, \mathbf{Q}^d\}$ and grid parameters, we solve the power
 438 generation $\{\mathbf{P}, \mathbf{Q}\}$ and complex-form voltage $\{\mathbf{V}\}$ as follows:

$$\mathbf{AC-OPF:} \quad \min \quad \sum_{i \in \mathcal{N}} \sum_{k \in \mathcal{G}_i} c_{i,k} \cdot P_{i,k}, \quad (5)$$

$$\begin{aligned}
& \text{s.t.} \\
\text{Power flow balance} \quad & \begin{cases} \sum_{k \in \mathcal{G}_i} P_{i,k} - P_i^d = \operatorname{re} \left(V_i \left(\sum_{j \in \mathcal{N}} Y_{ij} V_j \right)^* \right) \\ \sum_{k \in \mathcal{G}_i} Q_{i,k} - Q_i^d = \operatorname{im} \left(V_i \left(\sum_{j \in \mathcal{N}} Y_{ij} V_j \right)^* \right) \end{cases}, \quad \forall i \in \mathcal{N}, \quad (6) \\
\text{Line power flow limits} \quad & |V_i \left((V_i - V_j) Y_{ij} \right)^*| \leq S_{ij}^{\max}, \quad \forall (i, j) \in \mathcal{L}, \quad (7) \\
\text{Generations limits} \quad & P_{i,k} \in [P_{i,k}^{\min}, P_{i,k}^{\max}], Q_{i,k} \in [Q_{i,k}^{\min}, Q_{i,k}^{\max}], \quad \forall i \in \mathcal{N}, \quad \forall k \in \mathcal{G}_i, \quad (8) \\
\text{Voltage limits} \quad & |V_i| \in [V_m^{\min}, V_m^{\max}], |\angle V_{ij}| \leq V_a^{\max}, \quad \forall i \in \mathcal{N}, \quad \forall (i, j) \in \mathcal{L}, \quad (9) \\
\text{var.} \quad & \mathbf{P}, \mathbf{Q}, \text{ and } \mathbf{V}.
\end{aligned}$$

439 The objective function in (5) represents total generation cost, calculated as a linear
440 function of power generation and individual generator costs ($c_{i,k}$). The non-linear
441 power flow balance constraints in (6) ensure power injection and load are balanced at
442 each bus, where Y_{ij} is the transmission line admittance. The line flow limits (S_{ij}^{\max}) in
443 (7) enforce thermal limits of transmission lines under static conditions. Operating lim-
444 its for power generation ($P_{i,k}^{\min}, P_{i,k}^{\max}, Q_{i,k}^{\min}, Q_{i,k}^{\max}$), voltage magnitude (V_m^{\min}, V_m^{\max}),
445 and voltage angles (V_a^{\max}) are specified in (8)–(9).

446 Compared with Linear or DC-OPF formulations [37], which neglect temperature-
447 dependent resistance and Joule heating losses in transmission lines, AC-OPF more
448 accurately captures the physical behavior of power transmission systems [38] and
449 enables the incorporation of heat flow analysis.

450 **OPF under Heatwaves.** Standard AC-OPF neither incorporates the impact of
451 weather on the electrical network's parameters, such as resistance, nor the dynamic
452 thermal limits of transmission lines. Temperature-Dependent AC Optimal Power Flow
453 (TD-OPF) [14, 38, 39] extends it by incorporating heat flow equations and temperature
454 constraints in Sec. 1.4. AC-based TD-OPF is formulated as follows:

$$\begin{aligned}
\text{TD-OPF:} \quad & \min \quad (5) \\
& \text{s.t.} \\
\text{ACOPF constraints} \quad & (6) - (9), \\
\text{Heat flow constraints} \quad & (2) - (4), \quad \forall l = (i, j) \in \mathcal{L}, \\
\text{Line current flow} \quad & I_l = |(V_i - V_j) Y_{ij}|, \quad \forall l = (i, j) \in \mathcal{L}, \quad (10) \\
\text{Line admittance} \quad & Y_l = 1/(R_l + i \cdot X_l), \quad \forall l = (i, j) \in \mathcal{L}, \quad (11) \\
\text{var.} \quad & \mathbf{P}, \mathbf{Q}, \text{ and } \mathbf{V}.
\end{aligned}$$

455 In this formulation, standard AC-OPF constraints and heat flow constraints are
456 coupled through line current magnitude in (10) and temperature-dependent line admitt-
457 ance in (11), where R_l is the line resistance and X_l is the line reactance. The current
458 flow generates Joule heating H_J , which increases conductor temperatures. The con-
459 straints from (2) to (4) model heat transfer in individual transmission line segments
460 under varying local weather conditions, ensuring permissible steady-state conductor
461 temperatures that determine line current-carrying capacities. The interdependence of
462 electrical and thermal constraints in the TD-OPF model more accurately captures
463 physical grid behavior than linearized models during heatwaves.

464 **Load Shedding Analysis.** We implement all operational constraints as hard con-
465 straints in our optimization formulation, ensuring that transmission line flows cannot
466 exceed the specified limits (whether 70% or 100% of thermal capacity). To assess grid

467 bottlenecks under safety operation conditions, we introduce slack variables representing
468 load shedding in the power balance equations and add a large penalty term for
469 load shedding in the objective function. This approach allows the model to identify
470 when and where the grid cannot meet demand while respecting security constraints,
471 providing quantitative measures of grid vulnerability during heatwave events.

472 **Security Contingency Analysis.** Beyond modeling weather-induced thermal
473 limits in AC-based TD-OPF, N-1 security constraints are widely implemented to
474 enhance grid operation robustness by ensuring system stability following any single
475 line outage [40]. These constraints require that all operational limits remain satisfied in
476 both the base case and all post-contingency states. The base case and post-contingency
477 states are coupled through generator ramping constraints: preventive formulations fix
478 real power generation dispatch across all states, while corrective formulations permit
479 decision variables to adjust within prescribed ranges following contingency occurrence.

480 Computational complexity scales linearly with the number of contingencies,
481 motivating research into simplified security constraint formulations. Two common
482 approaches prevail in the literature. The first applies a fixed percentage reduction (e.g.,
483 70%) to thermal limits within AC-OPF models, establishing implicit safety margins
484 without explicit contingency enumeration [37]. The second integrates linearized secu-
485 rity constraints based on Line Outage Distribution Factors (LODFs) to approximate
486 contingency impacts within DC-OPF frameworks [41].

487 We adopt different approaches depending on system scale and data availability.
488 For the IEEE 30-bus test system (Supplementary Section 3), we implement standard
489 N-1 preventive security-constrained AC-OPF under heatwave conditions, leveraging
490 its complete topology and system parameters while maintaining computational feasi-
491 bility. For larger-scale European country-level analysis, we adopt the established 70%
492 fixed security margin approach from PyPSA-Eur [37]. This choice reflects two practi-
493 cal constraints: network clustering introduces an incomplete topology that precludes
494 rigorous contingency definition, and explicit contingency modeling at a continental
495 scale imposes a prohibitive computational burden for AC-based formulations.

496 **Impact of Storage and State of Charge.** The expanding deployment of dis-
497 tributed energy storage offers potential for mitigating local capacity constraints and
498 absorbing renewable generation variability through strategic charging and discharg-
499 ing. However, directly incorporating these temporal dynamics into AC-based TD-OPF
500 presents significant methodological challenges: Solutions become dependent on state-
501 of-charge initialization, require extended time horizons spanning days to years to
502 capture storage behavior under variable weather conditions, and substantially increase
503 computational complexity.

504 To balance analytical rigor with computational tractability, we adopt a simplified
505 approach. Using existing storage infrastructure configurations from PyPSA-Eur-
506 derived grid data (see Supplementary Table 5 for details), we implement a baseline
507 scenario assuming 50% initial state of charge—a moderate assumption representing
508 typical operational conditions. We complement this baseline with comprehensive sen-
509 sitivity analyses across the full range of storage states (0%–100%) to characterize how
510 storage availability affects system vulnerability. Results show that even at 100% state

511 of charge, storage provides only marginal relief from load shedding (Fig. 4d), indicating
 512 that transmission constraints—not storage capacity—dominate grid vulnerability
 513 during extreme heat. Under this framework, storage units function as dispatchable
 514 generators in our single-snapshot analysis of extreme heatwave conditions.

515 The comprehensive problem formulations for different OPF problems are included
 516 in Supplementary Section 2.

517 1.6 Algorithm Design

518 For standard AC-OPF, Interior Point Methods (IPMs) have demonstrated effectiveness
 519 across various IEEE test scenarios [23, 42]. Extending these methods to solve
 520 AC-based TD-OPF markedly increases complexity due to the interdependence of
 521 electrical and thermal constraints.

522 Existing Algorithms

523 Existing studies adopt different approximation methods to solve AC-based TD-OPF

- 524 • Linear approximation (DC-OPF and TD-DC-OPF): This approach linearizes the
 525 nonlinear constraints in AC-OPF and incorporates weather-dependent dynamic line
 526 ratings [13, 14, 43]. However, it generally overlooks the interactions between heat
 527 flow and power flow, leading to substantial inaccuracies in the resolved power flows.
- 528 • Quadratic approximation (Quad-OPF): It uses a quadratic function to estimate
 529 steady-state conductor temperature [15], expressed as $T_c \approx \beta_0 + \beta_1 I^2 + \beta_2 I^4$
 530 with weather-dependent coefficients $\{\beta_0, \beta_1, \beta_2\}$. This simplified version of the heat
 531 balance equation is then integrated into the standard AC-OPF model.

532 While these approximations enhance computational efficiency, they often fail to fully
 533 satisfy physical constraints on heat and power balance equations, particularly under
 534 stringent temperature-induced thermal constraints. These methods frequently over-
 535 look potential capacity constraints, resulting in inaccuracies when evaluating grid
 536 performance under extreme weather scenarios.

537 Despite these advancements, developing an efficient algorithm capable of solving
 538 AC-based TD-OPF models while satisfying all physical constraints has been a
 539 significant gap that we address in this work.

540 Proposed Iterative Analysis (Iter-OPF)

541 In this work, we propose a novel iterative framework for efficiently solving AC-based
 542 TD-OPF. As illustrated in Figure 2b and detailed in Algorithm 1, this algorithm
 543 employs two key steps that improve computational efficiency and solution accuracy.

- 544 • First, we convert steady-state conductor temperature constraints into equivalent
 545 conductor current constraints based on local segment weather conditions [13, 43]:

$$I_{l,s}^{\max} = \sqrt{(H_C + H_R - H_S)/(R(T^{\max}))}, \forall l = (i, j) \in \mathcal{L}, \forall s \in \mathcal{S}_l \quad (12)$$

$$I_l = |(V_i - V_j)Y_{ij}| \leq \min_{s \in \mathcal{S}_l} \{I_{l,s}^{\max}\}, \forall l = (i, j) \in \mathcal{L} \quad (13)$$

Algorithm 1 Iter-OPF Analysis

Data: Weather data, conductor thermal model, and power grid model.
Result: Grid operational states under heatwaves.

- 1 For each segment, given the gridded weather data, transform the temperature limit to the current constraint as Equation (12).
- 2 For each line, select the minimum current limit among segments as the line current constraint as Equation (13).
- 3 **while** conductor temperature not converge **do**
 - 4 Update temperature-dependent admittance for every segment as Equation (11).
 - 5 Aggregate segment admittance into line admittance as Equation (4).
 - 6 Solve AC-OPF with updated admittance and current constraints (13) via IPOPT.
 - 7 Update the line current derived from the OPF analysis as Equation (10).
 - 8 Solve heat flow equations in (1) for all segments via Bisection methods.
 - 9 Update the segment temperature derived from heat flow equations.
- 10 **end**

546 This strictly enforces line thermal limits under temperature conditions while eliminating
547 explicit steady-state temperature expressions, effectively decoupling heat
548 and power balance equations.

549 • inspired by decoupling approaches for TD power flow equations [38, 44], we develop
550 an alternating update mechanism where (i) AC-OPF is solved with additional current
551 constraints from (13) and (ii) heat balance calculations are conducted in parallel
552 for each segment. Empirical evaluations indicate that two iterations typically achieve
553 results within 0.1% of fully converged solutions for both load shedding and line
554 temperature metrics.

555 By decoupling heat and power balance constraints, our algorithm enables flexible
556 and precise assessment of grid conditions under diverse thermal and electrical properties.
557 This approach fills a critical gap in OPF studies by efficiently solving AC-based
558 TD-OPF while maintaining physical accuracy, thereby enabling rigorous grid analysis
559 for policy decisions during extreme weather events. As climate variability increasingly
560 threatens grid stability, such tools become essential for utilities to predict and mitigate
561 thermal stress on transmission systems.

562 European Simulation Overview

563 To investigate European electricity grid resilience under projected future heatwaves,
564 we integrate grid and weather data using our modeling framework to conduct OPF
565 analysis for Western Europe, with detailed settings in [Supplementary Section 4](#).

566 We focus on eight Western European countries (Spain, Portugal, France, Italy,
567 Germany, Belgium, the Netherlands, and the UK) impacted by historically recorded
568 heatwaves in 2019 and 2022 ([Supplementary Table 3](#)). Using the PyPSA-Eur frame-
569 work, we derive the power grid configurations detailed in [Supplementary Table 4](#) and
570 [Supplementary Table 5](#).

571 For network resolution, we adopt a clustered grid that merges nearby buses and
572 lines to mitigate local modeling inaccuracies, such as mis-assignment of loads and

573 under-representation of underground cabling, reducing error-induced bottlenecks [16].
574 All under-construction lines are included to enhance grid connectivity and provide a
575 more optimistic assessment of capacity under stress [16]. We standardize transmission
576 lines to “Al/St 240/40 4-bundle 380.0” (Aluminium/Steel cross-section 240/40 mm², 4-
577 bundle configuration at 380 kV) [16, 45]. Thermal limits are set at 90°C for Aluminium-
578 type conductors, within the typical 80–120°C operating range [15, 35, 46–49].

579 Since PyPSA-Eur data are designed for DC/linear dispatch models, we augment
580 them for OPF simulations. Voltage magnitude is constrained to $0.95 \leq V_m \leq 1.05$
581 following grid standards [23]. Reactive power demand is set proportional to active
582 power ($Q_d = 0.15 \cdot P_d$) following EnerPol recommendations [50]. We relax other AC-
583 OPF constraints, such as reactive generation capacity and branch phase angle limits,
584 as this information is not available in existing generator profiles [13].

585 In summary, our model adopts a conservative approach by using an aggregated
586 network topology with relaxed constraints, enabling exploration of upper limits of
587 grid performance and identification of potential bottlenecks under extreme conditions.
588 These insights pinpoint areas requiring more stringent controls under actual opera-
589 tion. Our framework can also incorporate additional constraints with realistic data for
590 more accurate evaluations, as demonstrated by exact solutions for the IEEE 30-bus
591 benchmark (Supplementary Section 3) alongside the EU analysis.

592 Author contributions

593 S.K. and M.C. conceived the study. E.L. collected the data for motivation and experi-
594 ments. E.L., M.C., and S.K. developed the formulation. E.L. developed the algorithm.
595 E.L. conducted the experiments. E.L., M.C., and S.K. analyzed the algorithm per-
596 formance and experimental results. E.L., M.C., and S.K. wrote and improved the
597 manuscript.

598 Data availability

599 The results from the model that support the findings of this study are presented in the
600 main text and Supplementary Information. The data used for validation are publicly
601 available from the sources in [Supplementary Table 1](#).

602 Code availability

603 The Iter-OPF algorithm developed in this study is available in the GitHub repos-
604 itory (<https://emliang.github.io/HEAT-GRID/webpage/>). The code is implemented
605 in Python and can be accessed for replication and further research.

606 References

607 [1] Ieee standard for calculating the current-temperature relationship of bare over-
608 head conductors. *IEEE Std 738-2012 (Revision of IEEE Std 738-2006 -*
609 *Incorporates IEEE Std 738-2012 Cor 1-2013)* 1–72 (2013).

610 [2] IPCC. *Climate Change 2021: The Physical Science Basis. Contribution of Working Group I to the Sixth Assessment Report of the Intergovernmental Panel on Climate Change* (Cambridge University Press, Cambridge, United Kingdom and New York, NY, USA, 2021).

611

612

613

614 [3] Perkins-Kirkpatrick, S. & Lewis, S. Increasing trends in regional heatwaves. *Nature Communications* **11**, 3357 (2020).

615

616 [4] Miranda, N. D. *et al.* Change in cooling degree days with global mean temperature rise increasing from 1.5° c to 2.0° c. *Nature Sustainability* **6**, 1326–1330 (2023).

617

618 [5] Vautard, R. *et al.* Heat extremes in western europe increasing faster than simulated due to atmospheric circulation trends. *Nature Communications* **14**, 6803 (2023).

619

620

621 [6] Ballester, J. *et al.* Heat-related mortality in Europe during the summer of 2022. *Nature Medicine* **29**, 1–10 (2023).

622

623 [7] Liu, L. *et al.* Climate change impacts on planned supply–demand match in global wind and solar energy systems. *Nature Energy* **8**, 1–11 (2023).

624

625 [8] Sun, Y. *et al.* Global supply chains amplify economic costs of future extreme heat risk. *Nature* **627**, 797–804 (2024).

626

627 [9] Dumas, M., Kc, B. & Cunliff, C. I. Extreme weather and climate vulnerabilities of the electric grid: A summary of environmental sensitivity quantification methods. Tech. Rep., Oak Ridge National Lab.(ORNL), Oak Ridge, TN (United States) (2019).

628

629

630

631 [10] Xu, L. *et al.* Resilience of renewable power systems under climate risks. *Nature Reviews Electrical Engineering* **1**, 53–66 (2024).

632

633 [11] You, J., Yin, F. & Gao, L. Escalating wind power shortages during heatwaves. *Communications Earth & Environment* **6**, 245 (2025).

634

635 [12] Ke, X., Wu, D., Rice, J., Kintner-Meyer, M. & Lu, N. Quantifying impacts of heat waves on power grid operation. *Applied energy* **183**, 504–512 (2016).

636

637 [13] Glaum, P. & Hofmann, F. Leveraging the existing german transmission grid with dynamic line rating. *Applied Energy* **343**, 121199 (2023).

638

639 [14] Neumann, F., Hagenmeyer, V. & Brown, T. Assessments of linear power flow and transmission loss approximations in coordinated capacity expansion problems. *Applied Energy* **314**, 118859 (2022).

640

641

642 [15] Ngoko, B. O., Sugihara, H. & Funaki, T. Optimal power flow considering line-conductor temperature limits under high penetration of intermittent renewable energy sources. *International Journal of Electrical Power & Energy Systems* **101**,

643

644

645 255–267 (2018).

646 [16] Hörsch, J., Hofmann, F., Schlachtberger, D. & Brown, T. Pypsa-eur: An open
647 optimisation model of the european transmission system. *Energy strategy reviews*
648 **22**, 207–215 (2018).

649 [17] Naumann, G. *et al.* Global warming and human impacts of heat and cold extremes
650 in the eu. *Crop Pasture Sci* **10**, 47878 (2020).

651 [18] Stone Jr, B. *et al.* How blackouts during heat waves amplify mortality and
652 morbidity risk. *Environmental Science & Technology* **57**, 8245–8255 (2023).

653 [19] Granskog, A., Hernandez Diaz, D. *et al.* The role of power in unlocking the
654 european ai revolution. *McKinsey & Company, October* **24**, 2024 (2024).

655 [20] Poudineh, R. Global electricity demand: What's driving growth and why it
656 matters (2025).

657 [21] Buontempo, C. *et al.* The copernicus climate change service: climate science
658 in action. *Bulletin of the American Meteorological Society* **103**, E2669–E2687
659 (2022).

660 [22] ENTSO-E. Opportunities for a more efficient European power system by 2050:
661 Infrastructure Gaps Report. Tech. Rep., European Network of Transmission
662 System Operators for Electricity (2025).

663 [23] Babaeinejadsarookolae, S. *et al.* The power grid library for benchmarking ac
664 optimal power flow algorithms. *arXiv preprint arXiv:1908.02788* (2019).

665 [24] Hersbach, H. *et al.* The era5 global reanalysis. *Quarterly journal of the royal*
666 *meteorological society* **146**, 1999–2049 (2020).

667 [25] Copernicus Climate Change Service. Climate and energy indicators
668 for europe from 2005 to 2100 derived from climate projections (2021).
669 URL [https://cds.climate.copernicus.eu/datasets/sis-energy-derived-projections?](https://cds.climate.copernicus.eu/datasets/sis-energy-derived-projections?tab=overview)
670 `tab=overview`. Accessed: 2024-10-06.

671 [26] Hirth, L., Mühlenpfordt, J. & Bulkeley, M. The entso-e transparency platform—a
672 review of europe's most ambitious electricity data platform. *Applied energy* **225**,
673 1054–1067 (2018).

674 [27] Staffell, I., Pfenninger, S. & Johnson, N. A global model of hourly space heating
675 and cooling demand at multiple spatial scales. *Nature Energy* 1–17 (2023).

676 [28] Hofmann, F., Hampp, J., Neumann, F., Brown, T. & Hörsch, J. Atlite: a
677 lightweight python package for calculating renewable power potentials and time
678 series. *Journal of Open Source Software* **6**, 3294 (2021).

679 [29] Eames, M., Kershaw, T. & Coley, D. A comparison of future weather created
 680 from morphed observed weather and created by a weather generator. *Building*
 681 and *Environment* **56**, 252–264 (2012).

682 [30] Herrera, M. *et al.* A review of current and future weather data for building
 683 simulation. *Building Services Engineering Research and Technology* **38**, 602–627
 684 (2017).

685 [31] Chan, A. Developing future hourly weather files for studying the impact of climate
 686 change on building energy performance in hong kong. *Energy and Buildings* **43**,
 687 2860–2868 (2011).

688 [32] Linnerud, K., Mideksa, T. K. & Eskeland, G. S. The impact of climate change
 689 on nuclear power supply. *The Energy Journal* **32**, 149–168 (2011).

690 [33] Elsebaay, A., Adma, M. A. A. & Ramadan, M. Analyzing the effect of ambi-
 691 ent temperature and loads power factor on electric generator power rating.
 692 *International Journal of Energy and Power Engineering* **11**, 171–176 (2017).

693 [34] Yang, W. *et al.* Thermal analysis for multi-conductor bundle in high voltage over-
 694 head transmission lines under the effect of strong wind. *Electric Power Systems*
 695 *Research* **231**, 110308 (2024).

696 [35] ENTSO-E. Technologies for transmission system. Technical Report, Euro-
 697 pean Network of Transmission System Operators for Electricity (2018).
 698 URL <https://eepublicdownloads.blob.core.windows.net/public-cdn-container/clean-documents/tyndp-documents/TYNDP2018/consultation/Technical/Technologies4TS.pdf>. TYNDP 2018.

701 [36] Cain, M. B., O’neill, R. P., Castillo, A. *et al.* History of optimal power flow and
 702 formulations. *Federal Energy Regulatory Commission* **1**, 1–36 (2012).

703 [37] Brown, T., Hörsch, J. & Schlachtberger, D. Pypsa: Python for power system
 704 analysis. *arXiv preprint arXiv:1707.09913* (2017).

705 [38] Frank, S., Sexauer, J. & Mohagheghi, S. Temperature-dependent power flow.
 706 *IEEE Transactions on Power Systems* **28**, 4007–4018 (2013).

707 [39] Ahmed, A., McFadden, F. J. S. & Rayudu, R. Weather-dependent power flow
 708 algorithm for accurate power system analysis under variable weather conditions.
 709 *IEEE Transactions on power systems* **34**, 2719–2729 (2019).

710 [40] Capitanescu, F. *et al.* State-of-the-art, challenges, and future trends in security
 711 constrained optimal power flow. *Electric power systems research* **81**, 1731–1741
 712 (2011).

713 [41] Hörsch, J., Ronellenfitsch, H., Witthaut, D. & Brown, T. Linear optimal power
714 flow using cycle flows. *Electric Power Systems Research* **158**, 126–135 (2018).

715 [42] Kocuk, B. *Global optimization methods for optimal power flow and transmission*
716 *switching problems in electric power systems*. Ph.D. thesis, Georgia Institute of
717 Technology (2016).

718 [43] Khaki, M., Musilek, P., Heckenbergerova, J. & Koval, D. *Electric power system*
719 *cost/loss optimization using dynamic thermal rating and linear programming*, 1–6
720 (IEEE, 2010).

721 [44] Ahmed, A., Massier, T., McFadden, F. S. & Rayudu, R. *Weather-dependent ac*
722 *power flow algorithms*, 1–8 (IEEE, 2020).

723 [45] Neumann, F. & Brown, T. *Heuristics for transmission expansion planning in*
724 *low-carbon energy system models*, 1–8 (IEEE, 2019).

725 [46] Nigol, O. & Barrett, J. Characteristics of acsr conductors at high tempera-
726 tures and stresses. *IEEE Transactions on Power Apparatus and Systems* 485–493
727 (1981).

728 [47] Douglass, D. & Reding, J. Ieee standard for calculating the current-temperature
729 of bare overhead conductors. *IEEE Standard 738–2006* (2007).

730 [48] Abboud, A. W., Gentle, J. P., Parikh, K. & Coffey, J. Sensitivity effects of
731 high temperature overhead conductors to line rating variables. Tech. Rep., Idaho
732 National Lab.(INL), Idaho Falls, ID (United States) (2020).

733 [49] Ngoko, B., Sugihara, H. & Funaki, T. *A temperature dependent power flow model*
734 *considering overhead transmission line conductor thermal inertia characteristics*,
735 1–6 (IEEE, 2019).

736 [50] Eser, P., Singh, A., Chokani, N. & Abhari, R. S. Effect of increased renewables
737 generation on operation of thermal power plants. *Applied Energy* **164**, 723–732
738 (2016).